Characterization and limits of a cold-atom Sagnac interferometer

A. Gauguet,[*] B. Canuel,[†] T. Lévèque, W. Chaibi,[‡] and A. Landragin[§]

LNE-SYRTE, Observatoire de Paris, CNRS, UPMC, 61 Avenue de l'Observatoire, 75014 Paris, France
(Received 10 July 2009; published 1 December 2009)

We present the full evaluation of a cold-atom gyroscope based on atom interferometry. We have performed extensive studies to determine the systematic errors, scale factor and sensitivity. We demonstrate that the acceleration noise can be efficiently removed from the rotation signal, allowing us to reach the fundamental limit of the quantum projection noise for short term measurements. The technical limits to the long term sensitivity and accuracy have been identified, clearing the way for the next generation of ultrasensitive atom gyroscopes.

I. INTRODUCTION

Inertial sensors are of interest in both science and industry. High precision sensors find scientific applications in the areas of general relativity [1], geophysics [2], and navigation [3]. In these fields, matter-wave interferometry is promising since it is expected to be an extremely sensitive probe for inertial forces [4]. In 1991, atom interferometry techniques were used in proof-of-principle demonstrations to measure rotations [5] and accelerations [6]. The first demonstrations of highly sensitive atomic gyroscopes using thermal beams [7,8] were obtained in 1997, followed by sensors with sensitivities at the state-of-the-art level [9,10]. For practical applications, cold-atom interferometry is of fundamental interest thanks to its intrinsic stability and accuracy, as the measurement of inertial forces is realized with respect to the inertial frame of the free-falling atoms. The use of cold atoms allows better control of atomic velocity and interaction time, leading to a better accuracy in a much more compact instrument [11–14].

In this paper we present the full characterization of a gyroscope based on atom interferometry, sensitive to the Sagnac effect. Different parameters have been taken into account for the study: the short term noise, the stability of the systematic effects, the scale factor, and its linearity. The apparatus uses cesium atoms and Raman transition to manipulate the matter wave packets. In our setup, we use a single Raman beam interacting with slow atoms, which makes the setup very versatile. Thus the experiment enables us to measure the full basis of inertia (three components of acceleration and rotation) with the same apparatus [11], making it suitable for applications such as inertial navigation. In this paper, we emphasize the possibility to measure the systematic effects and the scale factor accurately thanks to our polyvalent apparatus. In Sec. II we describe the experimental setup and the

measurement process. A detailed analysis of the different sources of systematic errors and tests of the scaling factor are presented in Sec. III. Finally, the analysis of the stability of the rotation measurement and its main limitations are described in Sec. IV.

II. APPARATUS

A global view of the experimental setup is presented in Fig. 1. The whole experiment is surrounded by two layers of mu-metal shield in order to reduce the impact of external magnetic fields. Cesium atoms are first loaded from a vapor into two independent magneto-optical traps (MOT), called A and B in the following. The two cesium clouds are then launched into two opposite parabolic trajectories using the moving molasses technique. At the top of their trajectory, the atoms interact successively three times with a unique pair of retro-reflected Raman beams, which acts on matter waves as beam splitters or mirrors. This creates an interferometer of 80 ms total maximum interaction time. The atomic phase shift is then obtained from the population in each output port, which is measured by a fluorescence technique thanks to the
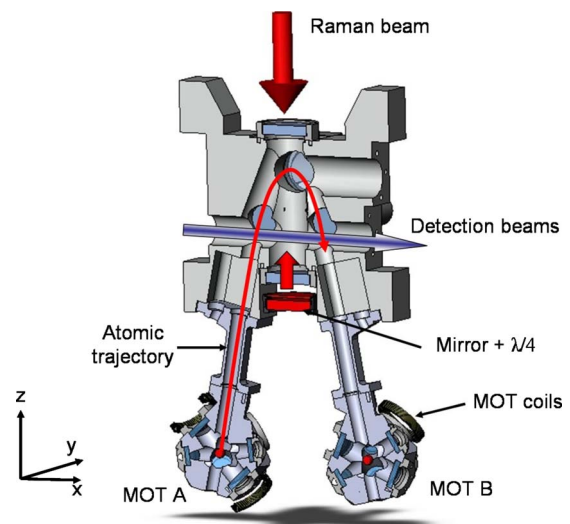

FIG. 1. (Color online) Scheme of the vacuum chamber showing the two MOTs, the interferometer zone and detection probe. The total dimensions of the system are $30 \times 10 \times 50$ cm^3.

---

*Present address: Department of Physics, Durham University, Rochester Building, South Road, Durham DH1 3LE, England.

†Present address: European Gravitational Observatory, Via E. Amaldi, 56021 S. Stefano a Macerata–Cascina (PI), Italy.

‡Present address: ARTEMIS–Observatoire de Nice, Boulevard de l'Observatoire, 06305 Nice, France.

§arnaud.landragin@obspm.fr

state labeling of the interferometer output ports [15].

In this paper we will focus on the configuration based on vertical Raman beams. The use of two atomic sources allows us to discriminate between the acceleration along the vertical direction and the rotation around the y horizontal axis. The experiment is mounted on a horizontal rotating platform, which enables us to vary the projection of the Earth's rotation rate along the sensitive axis of the gyroscope.

A. Atomic preparation

Cesium atoms are loaded from a thermal vapor during 140 ms into two independent MOTs. After the MOT coils are turned off, the atoms are kept in an optical molasses for 15 ms, to allow the stray magnetic field to decay. A frequency shift between the upper and the lower cooling beams is then applied, to launch the atoms thanks to the moving molasses technique. The independent control of the lower and upper cooling beam frequencies is achieved by passing through two different acousto-optic modulators (AOM). By applying a frequency shift of 3.2 MHz on the AOM controlling the lower cooling beams, the atoms are launched with a velocity of 2.4 m s^{-1} at an angle of 8° with respect to the vertical direction. In addition, the atoms are cooled down to a temperature of about 1.2 μK in the molasses by chirping the mean frequency down to -15Γ, with respect to the closed transition $|F=4\rangle \leftrightarrow |F'=5\rangle$.

Following this launching stage, the atoms are distributed among all Zeeman sublevels of the $|6S^{1/2}, F=4\rangle$ state. In order to reduce the sensitivity to parasitic magnetic fields, atoms are selected in the sublevel $m_F=0$. For this purpose, a static magnetic field of 30 mG is applied in the z direction to lift the degeneracy of the Zeeman sublevels. Atoms in $|6S^{1/2}, F=4, m_F=0\rangle$ are transferred to $|6S^{1/2}, F=3, m_F=0\rangle$ when passing through a microwave cavity. Any atoms remaining in $|6S^{1/2}, F=4\rangle$ are then removed by means of a pusher beam. After this preparation stage, we obtain typically 10^7 atoms in the $|6S^{1/2}, F=3, m_F=0\rangle$ ground state with a residual in the other states of less than 1%, for both sources.

B. Implementation of the interferometer

1. Three pulse interferometer

When the atoms arrive close to the apex of the parabolic trajectories, occurring at $t_{ap}=244$ ms after launch, the wave packets are split, deflected, and recombined by stimulated Raman transitions [6] in order to realize the interferometer. Since the Raman beams are vertically oriented the interferometric area is created in the (x,z) plane (Fig. 2).

The output phase shifts $\Delta\Phi^A$ and $\Delta\Phi^B$ of the two interferometers are composed of three terms which depend, respectively, on the acceleration **a**, the rotation **Ω**, and the Raman laser phase differences of the three pulses [16],

$$\Delta\Phi^{A,B} = \Delta\Phi_a + \Delta\Phi_\Omega^{A,B} + \Delta\Phi_{laser}. \tag{1}$$

In the vertical Raman configuration studied here, these contributions are written as a function of the vertical accelera-
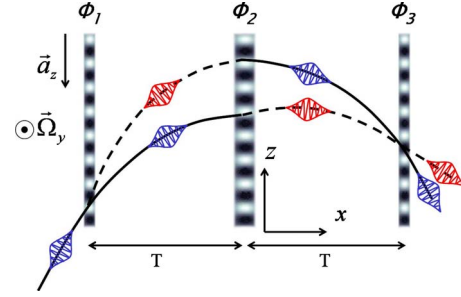

FIG. 2. (Color online) Scheme of the $\pi/2 - \pi - \pi/2$ interferometer in the vertical Raman configuration with a total interaction time of $2T$. The interferometer is sensitive to the vertical acceleration a_z and the rotation Ω_y. Solid and dotted lines, respectively, represent the partial wave packets in the states $|6S_{1/2}, F=3\rangle$ and $|6S_{1/2}, F=4\rangle$.

tion a_z, the horizontal rotation Ω_y and the Raman laser phase differences ϕ_i, $i=1,2,3$,

$$\Delta\Phi_a = k_{\text{eff}} a_z T^2,$$

$$\Delta\Phi_\Omega^{A,B} = 2\ k_{\text{eff}} V_x^{A,B} \Omega_y T^2,$$

$$\Delta\Phi_{laser} = \phi_1 - 2\phi_2 + \phi_3, \tag{2}$$

where $\mathbf{k}_{\text{eff}}$ is the effective wave vector of the Raman beam. The rotation phase shifts $\Delta\Phi_\Omega^{A,B}$ measured by the two interferometers are related to the horizontal velocities $V_x^{A,B}$ and have opposite signs for the two sources. The use of two counterpropagating sources allows to discriminate between the acceleration and rotation phase shifts [9].

2. Raman lasers

In order to drive Raman transitions between $|6S_{1/2}, F=3, m_F=0\rangle$ and $|6S_{1/2}, F=4, m_F=0\rangle$, two counterpropagating laser beams, with a frequency difference of 9.192 GHz, are required. These two optical frequencies are generated by two extended cavity laser diodes [17] emitting at $\lambda=852$ nm. The first laser is locked by frequency comparison to the MOT repumper beam with a detuning of 350 MHz with respect to the $|6S_{1/2}, F=3, m_F=0\rangle \leftrightarrow |6P_{3/2}\rangle$ transition. A second laser is phase locked to the previous one by comparing the beat note between the two beams with a microwave reference [18]. In order to get sufficient power to drive the transitions, the two laser beams are injected into a common semiconductor tapered amplifier (EYP-TPA-0850–01000–3006-CMT03) [19]. The power ratio between the two lasers is adjusted close to 0.5 in order to cancel the effect of the ac Stark shift (see part IIIC2). This ratio is then finely tuned by means of Raman spectroscopy on the cold-atom samples. After amplification, the two lasers have the same polarization and are guided to the atoms through the same polarizing fiber. At the output of the fiber, the beam is collimated with an achromatic doublet lens of 240 mm focal length, giving a diameter at $1/e^2$ of 35 mm. The intensity at the center of the beam is 20 mW cm^{-2}. The two counterpropagating beams are obtained thanks to a retro-reflected configuration in which the two frequency beam passes through the vacuum
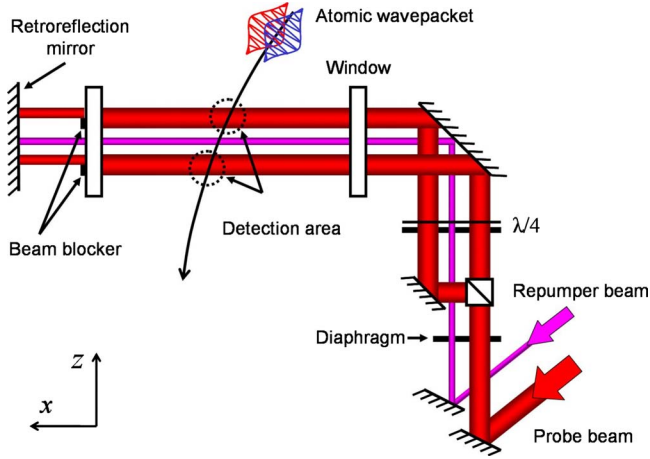
FIG. 3. (Color online) Scheme of the detection system. Two retro-reflected probe beams are generated from the same laser while a repumper beam is inserted between them. These three beams are shaped to form horizontal slices using two slits.

chamber and is reflected by a mirror, crossing a quarter-wave plate twice (Fig. 1). The quarter-wave plate is set in such a way that retro-reflected polarizations are orthogonal with respect to the incident ones. In this manner, counterpropagating Raman transitions are allowed while copropagating ones are forbidden. This retro-reflected configuration limits the parasitic effects induced by the wave-front distortions, which are critical in order to achieve good accuracy and long term stability (see Sec. III C 4).

Moreover, since the atoms are in free fall, the frequency difference between the two atomic levels is Doppler shifted in the vertical direction by $\omega_D = \mathbf{k}_{\mathrm{eff}} \cdot \mathbf{g}(t - t_{ap})$, which depends on the gravity g. In order to satisfy the resonance condition during the whole atomic flight, the frequency difference between the two Raman lasers is chirped thanks to a direct digital synthesizer (DDS). Additionally the interferometers are realized with a delay of 5 ms with respect to the apex of the trajectories in order to avoid a null Doppler shift during the π pulse.

C. Detection system

1. Detection apparatus

With Raman transitions, state labeling [15] enables one to determine the momentum state of the atoms by measuring their internal state. Thus, the phase shift of the interferometer can be obtained simply by measuring the transition probability of the atoms between the two ground states $|6S_{1/2}, F = 3, m_F = 0\rangle$ and $|6S_{1/2}, F = 4, m_F = 0\rangle$ at the output of the interferometer. The population measurement is performed by counting the number of fluorescence photons emitted by the atoms at the crossing of successive resonant laser beams. These beams are shaped to form horizontal slices of light with a rectangular section of 10×5 mm so as to probe the whole atomic clouds.

The detection system is made up of three counter propagating beams circularly polarized as shown in Fig. 3. The upper and lower beams are used as probes with a saturation

parameter of 0.3. They are obtained from the same laser, tuned to the closed atomic transition $|6S_{1/2}, F = 4\rangle \leftrightarrow |6P_{3/2}, F' = 5\rangle$. A repumper beam is inserted between these two probes and tuned to the transition $|6S_{1/2}, F = 3\rangle \leftrightarrow |6P_{3/2}, F' = 4\rangle$.

After the interferometric sequence, the atoms pass through the first probe. The fluorescence light emitted by the cycling transition $|6S_{1/2}, F = 4\rangle \leftrightarrow |6P_{3/2}, F' = 5\rangle$ is collected by an imaging system (3.7% efficiency) and focused onto a photodiode (Hamamatsu 1327BQ). The output signal s_1, given by the area of the time-of-flight signal, is proportional to the number of atoms projected into the $|6S_{1/2}, F = 4\rangle$ state. The lower part of this first probe beam is not retro reflected in order to eliminate these atoms. The remaining cloud, made up of atoms in the $|6S_{1/2}, F = 3\rangle$ ground state, is optically pumped to the $|6S_{1/2}, F = 4\rangle$ state while passing through the repumper beam. These atoms are finally detected with the second probe beam, providing a signal s_2 proportional to the number of atoms initially in the state $|6S_{1/2}, F = 3\rangle$ at the output of the interferometer. Each interferometer uses two imaging systems in order to collect the signal emitted by the atoms in the two respective ground states. The transition probability P is deduced from the fluorescence signals obtained on the two photodiodes (s_1 and s_2) and is written: $P = \frac{s_1}{s_1 + s_2}$.

2. Detection noise analysis

The noise affecting the fluorescence signals can be separated into three main contributions [20]. The first is related to power or frequency fluctuations of the probe beams that induce a noise which scales linearly with the total number of atoms N^A and N^B in each source. The second contribution consists of a technical noise related to the detection system (photodiode dark current and amplifier noise) that gives a contribution independent of the total number of atoms in the probe. Finally, the quantum projection noise (QPN) gives a fundamental limit of the measurement [21] and scales as $[P^{A,B}(1 - P^{A,B})N^{A,B}]^{1/2}$. These independent sources of noise can be added quadratically, giving a variance of the transition probability,

$$\sigma_{P^{A,B}}^2 = \alpha + \frac{P^{A,B}(1 - P^{A,B})}{N^{A,B}} + \frac{\gamma}{N^{A,B^2}}. \qquad (3)$$

In order to determine the parameters α and γ when working at one side of a fringe of the interferometer, we use a single Raman laser pulse giving an average transition probability close to 0.5. In such a case, the noise detection properties are similar to those of the interferometer without being sensitive to the interferometer phase noise. In practice, the Raman laser power is reduced so that the Raman pulse duration $\tau = \pi / \Omega_{Rabi}$ limits the average transition probability to $P^{A,B} = 0.5$ by velocity selection. By this means, the measurement is made almost insensitive to any power fluctuations of the Raman beam.

The detection noise σ_P is evaluated as a function of the number of detected atoms, which is changed by varying the loading time of the MOTs (see Fig. 4). The data are scaled as a function of the fluorescence signal $S = s_1 + s_2$, which is pro-
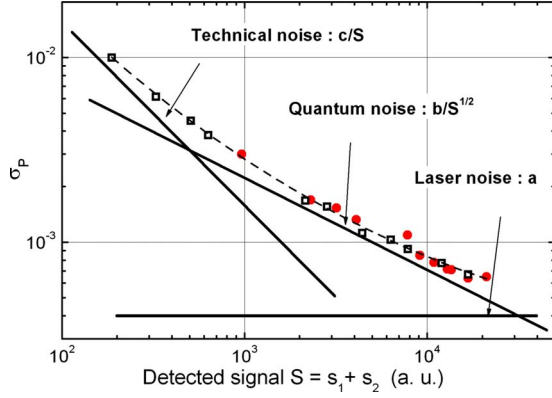
FIG. 4. (Color online) Detection noise analysis. The shot-to-shot Allan standard deviation of the transition probability is plotted versus the detected signal S in the same arbitrary unit for the two sources (respectively, black squares and red dots). The dashed curve corresponds to the fit of the data by the noise model, which can be separated into three terms corresponding to the three solid lines.
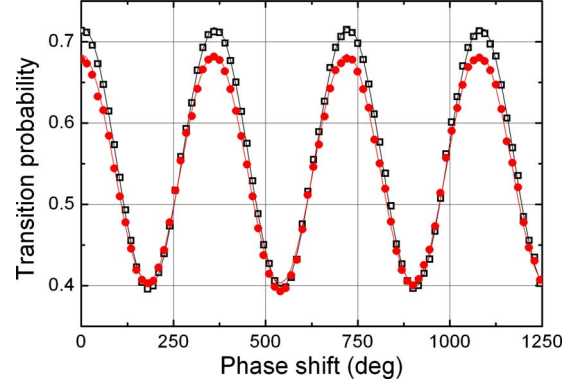

FIG. 5. (Color online) Atomic fringe patterns obtained for the interferometers A (black squares) and B (red dots) with an interaction time of $2T=80$ ms and a pulse duration of 13 μs. In order to scan the fringe patterns we incremented the effective Raman laser phase at each measurement cycle.

portional to the actual atom number $N^{A,B}=\eta S$. The two detection systems clearly show identical noises for the two atomic sources. A fit of the experimental data has been realized by Eq. (3) in which the scaling of the number of atoms is a free parameter. This leads to a fit with three parameters (a,b,c), related to α, γ, and η, which are reported in Table I. For the usual experimental parameters, the number of atoms detected corresponds to $S=7000$ and the signal to noise ratio is then limited by the quantum detection noise. In this case, the parameter b allows the determination of the actual number of atom detected for each source, giving $N=3.6 \times 10^5$ atoms, which is in agreement with additional measurements realized by absorption.

D. Measurement process

Interference fringe patterns are scanned by taking advantage of the Raman laser phase control. Indeed, by adding a laser phase offset $\delta\varphi_n$ between the second and the third pulses of the nth measurement, the atomic phase measured evolves as $\Delta\Phi_{laser}=\phi_1-2\phi_2+(\phi_3+\delta\varphi_n)$. In practice, the phase increment $\delta\varphi_n$ is applied to the microwave signal used as a reference to phase-lock the two Raman lasers. The fringe patterns, shown in Fig. 5, were obtained with the usual parameters, $2T=80$ ms and Raman pulse durations of $\tau =13$ μs. Both atomic sources exhibit a contrast C close to 30% mainly limited by the Raman transition efficiency. Two phenomena are responsible for this limitation. On the one hand, the atomic cloud velocity distribution is broader than

the velocity linewidth of the Raman transition. On the other hand, because of the thermal expansion of the atomic cloud, all the atoms do not experience the same laser power in the Gaussian Raman beam, and therefore do not experience the same Rabi frequency.

The transition probability measured at the output of the interferometer is written as a function of the following terms: an offset $M^{A,B}$, a contrast $C^{A,B}$, a phase shift due to inertial effects $\Delta\Phi_I^{A,B}$ (acceleration and rotation) and a laser phase shift $\Delta\Phi_{laser}$,

$$P^A = M^A + C^A \cos(\Delta\Phi_I^A + \Delta\Phi_{laser}),$$

$$P^B = M^B + C^B \cos(\Delta\Phi_I^B + \Delta\Phi_{laser}). \quad (4)$$

The phase shift accumulated by the two interferometers can then be deduced by fitting each fringe pattern with the Eq. (4). The acceleration and rotation phase shifts are then discriminated by calculating, respectively, the half sum and half-difference of the two fitted phase shifts,

$$\Delta\Phi_a = \frac{\Delta\Phi^A + \Delta\Phi^B}{2} \qquad \Delta\Phi_\Omega = \frac{\Delta\Phi^A - \Delta\Phi^B}{2}. \quad (5)$$

In the general case, the interferometric phase shift can always be extracted from four points: $\Delta\Phi_{laser}=0°$, $+90°$, $+180°$, and $270°$.

With the retro-reflected configuration, atoms are submitted to four laser waves which couple Raman transitions along two opposite effective wavevectors $\pm\mathbf{k}_{eff}$. The opposite Doppler shift between these two effective transitions allows the deflection of the atomic wave packets along one or the other direction by changing the sign of the frequency ramp delivered by the direct digital synthesizer. The sign of the inertial phase shifts $\Delta\Phi_I^{A,B}$ changes according to $\pm\mathbf{k}_{eff}$. Consequently, by processing the half-difference of the phase shift measured at $\pm\mathbf{k}_{eff}$, parasitic phase shifts independent of the direction of the effective wave vector are removed thanks to this k-reversal technique.

To sum up, the experimental sequence consists in acquiring transition probability measurements on the two sources,
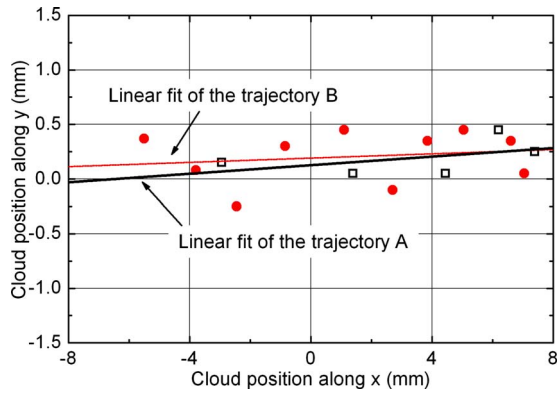
TABLE I. Table of the fitted parameters deduced from the measurement of the detection noise, presented in Fig. 4.

Noise	Fitted parameters	
Laser	$a=\sqrt{\alpha}$	$=4\times10^{-4}$
QPN	$b=1/(2\sqrt{\eta})$	$=7\times10^{-2}$
Technical	$c=\sqrt{\gamma}/\eta$	$=1.6$

FIG. 6. (Color online) Trajectories of the atomic clouds A (black squares) and B (red dots) in the xy plane, in the interaction area. Two linear fits of experimental data show that the overlap is better than 0.5 mm, limited by the measurement resolution.

alternately for each direction of the wave vector $\pm\mathbf{k}_{\mathrm{eff}}$. The fit is processed afterward and we infer a measurement of the inertial phase shifts for each set of eight acquisition points.

III. SYSTEMATIC ERRORS AND SCALE FACTOR

A. Characterization of the atomic trajectories

A crucial point, when measuring a differential phase shift between two interferometers [9,22,23], is the overlap of the two atomic trajectories. Indeed, if the trajectories are perfectly overlapped, many systematic effects cancel out, as explained in paragraph IIIC. Consequently, the two cold-atom sources were realized with particular care. In this section, we study both the overlap and the stability of the two trajectories.

1. Overlap of the atomic trajectories

When using Raman laser beams oriented in the vertical direction, the atomic trajectories have to be overlapped in the orthogonal plane (xy) since the Raman laser system remains invariant along the z direction. In addition, the two atomic clouds must be resonant simultaneously with the single Raman beams which implies that vertical velocities must be equal. The key parameters allowing to fulfill these requirements are the initial positions and velocities of the two atomic sources. Despite a careful alignment and power adjustment of the twelve trap laser beams, the overlap of the two trajectories has to be finely tuned. The adjustment of the velocities is achieved by modifying the launching directions (thanks to the tilt of the experiment) and by changing independently the values of the launch velocities. The relative positions at the moment of the Raman pulses were optimized by adjusting the timing sequence and the positions of the zeros of the quadratic magnetic fields in the two traps.

We directly map the two trajectories in the interferometer zone thanks to the Raman laser beams, with a movable aperture of diameter 5 mm. By maximizing the transfer efficiency of a Raman pulse, we deduce the actual position of each atomic cloud in the xy plane at a given time. Figure 6 shows the two trajectories which are overlapped to better
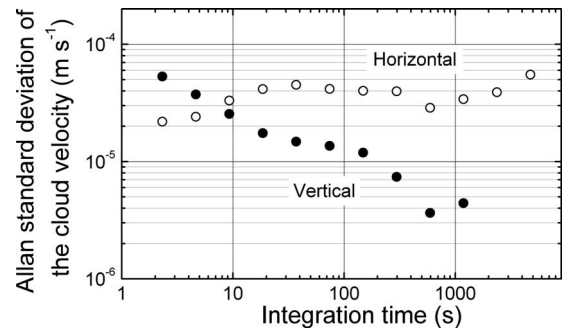

FIG. 7. Allan standard deviation of the atomic velocity for source A measured by Raman spectroscopy. The analysis is carried out from a 12 h continuous acquisition.

than 0.5 mm over the whole interferometer zone. The measurement resolution is limited by the spatial extension of the atomic clouds (5 mm FWHM at the apex).

2. Stability of the trajectory overlap

The stability of the overlap is of primary interest for the stability of the rotation rate measurements (paragraph IV). Ideally, independent measurements of the initial velocities and positions of the two sources in the (xy) plan should be performed. Unfortunately, the use of the time-of-flight method and Raman lasers along either the y or the z axes only gives access to the initial position stabilities in the z axis and velocities in the y and z directions. Nevertheless, this measurement gives an evaluation of the typical fluctuations of position and velocity which are needed in the analysis of the long term stability.

The atomic velocity stability is measured by Raman spectroscopy, using horizontal or vertical Raman laser beams. For counterpropagating Raman beams, the resonance condition depends on the Doppler effect and leads to a measurement of the atomic velocity. In addition, to discriminate the Doppler effect from other sources of frequency shift, we use the k-reversal method described in chapter IID. Figure 7 shows the Allan standard deviations of velocities along the z and y directions for source A. Similar behaviors have been recorded for source B, with stabilities between 2 and 30 μm s^{-1} for time scales from 1 to 5000 s. In addition, the fluctuations of the initial position along the vertical direction can be obtained by combining the previous velocity data with simultaneous time of flight measurements. Therefore we can estimate the Allan standard deviation of the initial position, which is 28 μm at 2 s, averaging over the long times (1000 s) to 15 μm. Combining these position and velocity fluctuations independently, we infer a typical overlap fluctuation of around 20 to 30 μm in the interferometer zone. In order to explain the sources of these fluctuations, additional studies have been performed. They demonstrate that relative power and polarization fluctuations of the opposing cooling beams can explain this result. Indeed, we measured a change of the launch velocity of 36 μm s^{-1} for 1% of polarization fluctuation and a initial displacement of 50 μm for 1% of intensity fluctuation between the three top and the three bottom cooling beams [24]. In normal operation, polarization
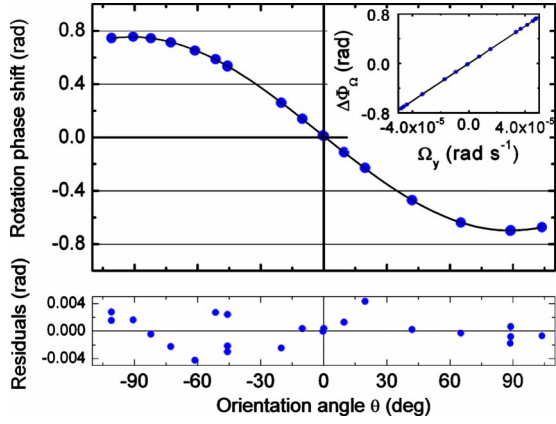
FIG. 8. (Color online) Measurement of the rotation phase shift as a function of the orientation θ of the experimental setup with respect to the east-west direction. Experimental data (dots) and their sinusoidal fit (line) are displayed on the top graph while their residuals are shown at the bottom. The inset exhibits the same data reported as a function of the rotation rate.

fluctuations are the dominant contributions affecting the stability of the trajectories.

B. Measurement of the systematic errors and the scale factor

In order to perform inertial force measurements, we need to know accurately the scale factors and the systematic errors, which link the actual rotation and acceleration quantities to the measured phase shifts $\Delta\Phi_{\rm rot}$ and $\Delta\Phi_{\rm acc}$. In order to determine these two parameters for rotation, we change, in a controlled way, the rotation rate measured by the gyroscope. In addition, taking advantage of the single Raman laser beam pair, the interaction time T can be changed continuously from $T=0$ to 40 ms. The systematic error and scale factor measurements were performed for various interaction times, giving a test of the quadratic scaling of the rotation phase shift with T.

1. Dependence on the rotation rate

The first test of the rotation scale factor consists in checking the proportionality between the rotation phase shift and

the rotation rate. For this purpose, the orientation θ between the sensitive axis of the gyroscope and the east-west direction, is changed to measure different horizontal projections of the Earth rotation rate, $\Omega_y = \Omega_h \sin\theta$. At the Observatoire de Paris, located at the latitude $\lambda = 48° \, 50' \, 08''$, the horizontal rotation rate Ω_h is 4.8×10^{-5} rad s^{-1}. The whole device is placed on a rotation mount, which determines the orientation with a relative accuracy of 50 μrad.

In Fig. 8 the rotation phase shift is plotted with respect to the orientation of the gyroscope. The experimental data are fitted by a sinusoidal function $\Delta\Phi = \Delta\Phi_\Omega^{er} + A^{(0)} \sin(\theta - \theta_0)$. The magnitude $A^{(0)}$ is used to calibrate the rotation scale factor: we find $A^{(0)}/(\Omega_T \sin\lambda) = 15124 \pm 12$ rad rad^{-1} s^{-1}. Moreover this measurement allows to deduce the systematic error of the rotation signal: $\Delta\Phi_\Omega^{er} = 28.3 \pm 0.7$ mrad.

The same data, when plotted as a function of the rotation rate, are well aligned with a slope equal to the scale factor. Nonlinearities appear as deviations to the straight line and can be evaluated by fitting with a quadratic term. Their relative contributions are below 10^{-5} in the range of measurement.

2. T scaling of the rotation phase shift

In order to test the T^2 scale factor dependence, the experimental setup is oriented at $\theta \simeq \pm 90°$, for which the sensitivity of the gyroscope to the Earth rotation is maximum. We also take advantage of the fact that, for these two orientations, an error in the orientation angle θ has a second-order effect on the rotation phase shift. Therefore we write

$$\Delta\Phi_\Omega^{+90°}(T) = \Phi_{rot}^{er}(T) - 2k_{\rm eff}V_x\Omega_yT^2,$$

$$\Delta\Phi_\Omega^{-90°}(T) = \Phi_{rot}^{er}(T) + 2k_{\rm eff}V_x\Omega_yT^2, \qquad (6)$$

where $\Phi_{rot}^{er}(T)$ is the systematic error on the rotation signal for a given interaction time T. The half-difference of the signal measured at $\theta = +90°$ and $\theta = -90°$ [Fig. 9(a)] gives a test of the scaling of the rotation phase shift as T^2. It shows excellent agreement with the expected behavior. In addition, the systematic error which affects the rotation signal is deduced from the half sum of the signals for the two orienta-
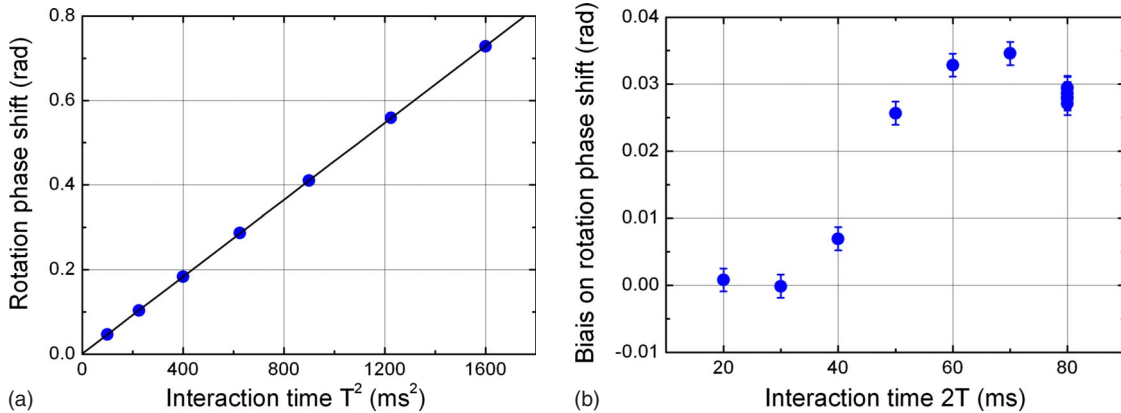

FIG. 9. (Color online) (a) Evaluation of the rotation phase shift versus the interaction time T^2. In this figure the systematic error is cancelled by the subtraction of the rotation signals obtained at $\pm 90°$. (b) Systematic error on the rotation signal as a function of the interaction time 2T. The systematic error is evaluated by calculating the half sum of the rotation signals measured at $\pm 90°$.
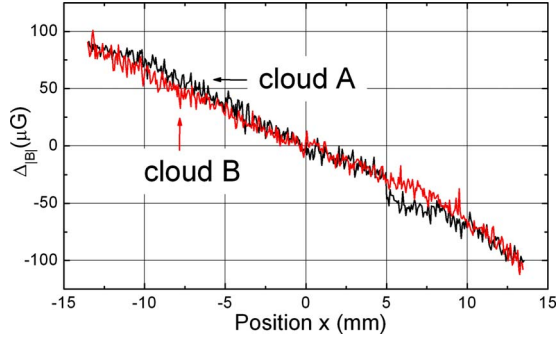
FIG. 10. (Color online) Measurement of the magnetic field as a function of the position of the atoms along their trajectory in the interaction zone.

tions. The evolution of the error phase shift is displayed as a function of the interaction time in Fig. 9(b). Negligible for small interaction times, it increases up to 34 mrad. For the usual interaction time of $2T=80$ ms, this systematic error reaches 28.3 mrad. The study of the different sources of systematic errors is performed in the following section.

C. Investigation of the sources of systematic errors

1. Quadratic Zeeman effect

The first expected source of systematic error in the interferometer phase shift comes from the Zeeman shift induced by the magnetic field. In order to limit its impact, the interferometer is realized between the two $m_F=0$ Zeeman sublevels, whose energy difference evolves quadratically with the magnetic field as $\Delta_{mag}=K^{(2)}B^2$, with $K^{(2)}=427.45$ Hz G^{-2} for cesium atoms. In addition, thanks to the symmetric features of the interferometer, the phase shift is not sensitive to a constant frequency shift. However, a magnetic field gradient breaks the symmetry and gives rise to a phase shift. Assuming a linear gradient δ_{bx} along the atomic trajectories the phase shift induced is

$$\Delta\Phi_{mag} = -4\pi K^{(2)}B_0 T^2 V_x \delta_{bx}. \tag{7}$$

The MOTs and the interaction region are set into three independent magnetic shields and the whole experiment is inside a second layer of shield so as to limit the influence of the ambient magnetic field. The magnitude of the residual magnetic field has been measured by selecting the atoms in the $m_F=2$ sublevel and driving magnetic transitions thanks to a microwave antenna. By measuring the frequency of the transition between the $|6S_{1/2},F=3,m_F=2\rangle$ and $|6S_{1/2},F'=4,m_{F'}=2\rangle$ states along the trajectories, we mapped the value of the magnetic field in the interaction zone. The results of these measurements are displayed in Fig. 10 for the two atomic clouds. We measured a gradient of $\delta_{bx}=7$ mG m^{-1} giving a small phase shift of 0.6 mrad on the rotation signal. This Zeeman phase shift does not depend on the laser wave vectors, therefore it cancels out with the k-reversal technique and so disappears on the total interferometer phase shift.

2. ac Stark shift

We study the effect of a frequency shift induced by the ac Stark shift Δ_{ac} on the interferometer phase shift [25]. This frequency shift between the two hyperfine levels can be cancelled by setting a proper intensity ratio between the two Raman beams. However, if the ratio is flawed, a phase shift $\Delta\Phi_{ac}$ is induced on the interferometer. Assuming the ac Stark shift to be constant during each laser pulse gives

$$\Delta\Phi_{AC} = \left(\frac{\Delta_{ac}^{(3)}}{\Omega_{eff}^{(3)}} - \frac{\Delta_{ac}^{(1)}}{\Omega_{eff}^{(1)}} \right) \tag{8}$$

where $\Delta_{ac}^{(1,3)}$ are the frequency shifts of the Raman transition at the time of the first and the third pulses, and $\Omega_{eff}^{(1,3)}$ are the respective effective Rabi frequencies [26]. In our experimental setup, the two Raman lasers are provided by a single optical fiber and are retro reflected, ensuring the stability of the intensity ratio between the two lasers throughout the Raman beam.

Equation (8) shows that if the atomic trajectories are perfectly overlapped and symmetric with respect to the center of the Raman beam, the phase shift $\Delta\Phi_{ac}$ remains equal to zero as the contributions of the first and last pulses are identical. However, a parasitic phase shift appears on the acceleration signal if the Gaussian profile of the Raman beam is not centered with respect to the three pulse sequence of the interferometer. A similar effect would be induced by time fluctuations of the laser power at the output of the fiber. Moreover, this phase shift also affects the rotation signal if the two trajectories are not perfectly superimposed.

The sensitivity of the rotation signal to the ac Stark shift was characterized by changing the intensity ratio between the two Raman lasers so as to induce a frequency shift of $\Delta_{ac}=10$ kHz. A sensitivity of 5 mrad kHz^{-1} was measured. This ac Stark shift is however independent of the effective wave vector $\mathbf{k}_{eff}$ so it can be rejected by the k-reversal method, considering that the fluctuation of $\Delta\Phi_{ac}$ is slow compared with the repetition rate of the measurement. Using this technique, we measure a residual error due to the ac Stark shift at the level of 0.1 mrad kHz^{-1} corresponding to a sensitivity to this effect reduced by a factor of 50. When running the interferometer, we directly optimize the ac Stark shift on the atomic signal with an accuracy better than 500 Hz, leading to a residual systematic error below 0.05 mrad which is negligible.

3. Two-photon light shift

As explained above the retro-reflected Raman beams couple the ground state $|6S_{1/2},F=3,\mathbf{p}\rangle$ with the two states $|6S_{1/2},F=4,\mathbf{p}\pm\hbar\mathbf{k}_{eff}\rangle$. Since these two possible Raman transitions are Doppler shifted, we can choose only one state by adjusting the Raman detuning. However, the nonresonant coupling induces a two-photon light shift (TPLS) on the selected Raman transition which results in an atomic phase shift ($\Delta\Phi_{TPLS}$) [27],

$$\Delta\Phi_{TPLS} = \frac{\Omega_{eff}^{(1)}}{4\delta_D^{(1)}} - \frac{\Omega_{eff}^{(3)}}{4\delta_D^{(3)}}, \tag{9}$$
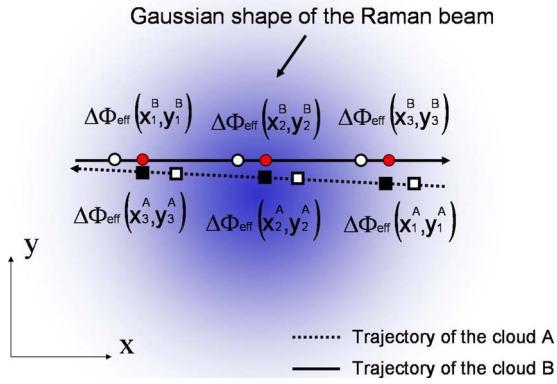
FIG. 11. (Color online) Wave-front defects induce a phase shift related to the laser phases seen by the atoms at the moments of the three laser pulses (black squares and red dots). By changing the moments when the pulses occur we simulate a relative displacement of the atomic clouds with respect to the Raman beam (white squares and white dots).

where $\Omega_{\text{eff}}^{(i)}$ is the effective Rabi frequency and $\delta_D^{(i)}$ the Doppler shift for the ith pulse. This phase shift depends on $\mathbf{k}_{\text{eff}}$ and cannot be cancelled out with the k-reversal method. It is shown that this shift is similar for the two interferometers and induces an error on the acceleration signal of only 12 mrad while remaining below 0.3 mrad on the rotation signal.

4. Wave-front distortion

The atomic phase shift depends on the effective laser phases ϕ_i imprinted on the atomic wave at the moments of the three pulses. Because of a nonuniform laser wave front, the phase shift measured by each interferometer depends on the position of the atomic cloud in the Raman wave front (x_i, y_i) at the ith pulse and can be written as

$$\Delta\Phi_{\text{wf}} = \phi_1(x_1, y_1) - 2\phi_2(x_2, y_2) + \phi_3(x_3, y_3). \quad (10)$$

The spatial variations of the laser phase along the wave-front induce a phase shift on the interferometric measurements. In our setup, the use of a retro-reflected configuration allows to reduce the number of optical elements and hence to decrease the aberrations between the two opposite Raman beams. Therefore, the wave-front defects are mainly induced by the Raman window, the quarter wave plate and the retro-reflection mirror, which affect only the reflected beam.

When the trajectories of the two atomic clouds are perfectly overlapped, the wave-front defects are identical for both interferometers, which is equivalent to a constant acceleration. If the paths are not perfectly overlapped, the phase shifts due to these wave-front defects are not identical and appear as an error on the rotation signal when subtracting the phase shifts of the two interferometers [28]. This is illustrated in Fig. 11, which represents the positions of the atomic clouds at the times of the three pulses $\pi/2 - \pi - \pi/2$. The error on the rotation signal results from the half-difference of the two wave-front distortion phase shifts: $\Delta\Phi_{\text{wf}} = \frac{\Delta\Phi_{\text{wf}}^A - \Delta\Phi_{\text{wf}}^B}{2}$.

A first estimation of this effect was performed by measuring the wave-front distortion induced by a single Raman
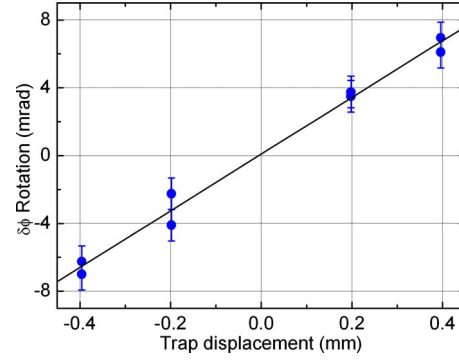

FIG. 12. (Color online) Rotation phase shift measured as a function of the atomic cloud positions along the x direction. The displacements of the atomic position compared to the laser beam are applied by changing the timing of the laser pulse sequence.

window with a Zygo wave-front analyzer [29]. From these measurements, we deduce a wave-front phase shift of 20 mrad on the rotation signal for an interaction time of $2T = 80$ ms, which is consistent with the error measured on the rotation signal. A second method was implemented to estimate this effect by moving the positions $(x_i, y_i)^{A,B}$ of the atomic clouds in the Raman beam at the moments of the pulses. This can be performed by changing the delay between the launch and the first Raman pulse, keeping the duration of the interferometer constant ($2T = 80$ ms). Consequently, the positions of the two atomic clouds are shifted in opposite directions, as shown on Fig. 11. In Fig. 12, the rotation phase is displayed as a function of the delay compared to the usual laser sequence, and translated into trajectory shift.

For small deviations, the phase shift due to wave-front defects can be linearized. Therefore we infer the sensitivity of the rotation measurement to a relative displacement along the x direction between the two sources by performing a linear fit of the data. The sensitivity obtained is

$$\frac{\Delta\Phi_{\text{wf}}}{\delta x} = 17 \ \mu\text{rad} \ \mu\text{m}^{-1}. \quad (11)$$

5. Conclusion on systematic errors

We studied the relative contributions of different sources of parasitic phase shifts. The dominant contribution to the systematic effects has been identified as coming from the wave-front distortions. Indeed, an independent evaluation of its contribution (~ 20 mrad) is in agreement with the actual parasitic phase shift (28.3 mrad) for $2T = 80$ ms [Fig. 9(b)]. This effect becomes significant when the interrogation time exceeds 30 ms. We attribute this to the growth of wave-front distortions on the edges of the windows. Using a larger window or the centers of three separated windows for the three pulses would limit its impact.

IV. SENSITIVITY

The bias stability of the acceleration and rotation signals was studied by orienting the area of the interferometer in the
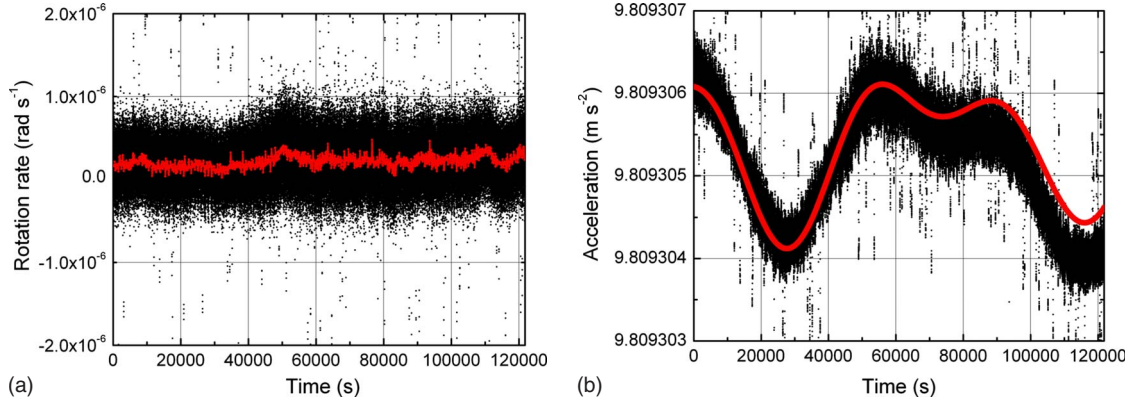
FIG. 13. (Color online) Rotation (a) and acceleration (b) measurements as a function of the time, obtained for an interaction time of $2T=80$ ms on a 34 h continuous acquisition. The rotation data (a) are presented shot-to-shot (black dots) and averaged over 100 s (red line). The shot-to-shot acceleration measurement (b) is compared to expected variations of the gravity (line) due to tidal effects.

east-west direction so that the rotation rate measured is zero. Consequently, it is possible to measure a phase shift by setting the interferometers on the side of the fringe for both interferometers simultaneously. Then we calculate the phase shift from the measured probabilities $P^{A,B}$, the contrast $C^{A,B}$ and the offsets $M^{A,B}$.

Since the interferometers operate at the side of a fringe, the fluctuations of the contrast parameters $C^{A,B}$ do not impact significantly the measured probabilities. Consequently, the contrast values are determined once at the beginning of the measurement, by fitting the fringe pattern with a sinusoidal function. To eliminate offset fluctuations, the experimental sequence alternates measurements on both sides of the central fringe. The half-difference between two successive measurements yields the atomic phase shift rejecting the offset fluctuations. Moreover, the sign of the effective wave vector $\mathbf{k}_{\mathrm{eff}}$ is reversed between two successive steps.

Figure 13 shows the two inertial signals as a function of time, for an interaction time of $2T=80$ ms and a repetition rate of 1.72 Hz. The large oscillations which appear on the acceleration signal are due to tidal effects and are removed on the rotation signal illustrating a key feature of our geometry. A more quantitative study of the separation between the acceleration and rotation signal demonstrated a 76 dB rejection rate, the details of this study are presented in Appendix. The efficiency of this rejection is due to the fact that the wave packets of the two sources interact with the same equiphase plane of the Raman beams at exactly the same time.

A. Acceleration measurements

The acceleration signal is deduced from the sum of the two interferometer phase shifts. The short term sensitivity obtained on these measurements is 5.5×10^{-7} m s^{-2} Hz$^{-1/2}$. This sensitivity is mainly limited by the residual vibrations of the platform, as for the atomic gravimeter [30]. The Allan standard deviation [Fig. 15(a)] of the acceleration signal shows an improvement of the sensitivity proportional to $\tau^{-1/2}$ as expected. By integrating our measurement over 5000 s, we reach a sensitivity of 10^{-8} m s^{-2}, which is close to our

atomic gravimeter characteristics presented in [30]. The difference between the sensitivity of the two apparatuses is explained by our slightly lower repetition rate and interrogation time. In order to reach this sensitivity, the noise contribution from vibrations is filtered out thanks to a passive isolation platform (nanoK 350BM-1). The residual noise is further reduced by a correlated measurement performed with a low noise seismometer (Guralp T40) [30]. Additionally, variations of the gravity g due to tidal effects are computed from a model provided by tide parameters extracted from [31] and subtracted from the signal in order to infer the long term stability of the sensor.

B. Noise on the rotation signal

The rotation phase shift is extracted from the difference between the signals of the two interferometers. The Allan standard deviation is plotted in Fig. 15(b). The short term sensitivity of the rotation signal is 2.4×10^{-7} rad s^{-1} Hz$^{-1/2}$. The Allan standard deviation decreases with integration time as $\tau^{-1/2}$, down to 1000 s, reaching a sensitivity of 10^{-8} rad s^{-1}.

The Allan standard deviation of the rotation signal at one second is limited by the quantum projection noise evaluated in Sec. II C 2. In order to confirm this point, we perform measurements for different numbers of atoms by changing the loading time of the two MOTs. Assuming that the detection noise is independent for the two interferometers A and B, its impact on the standard deviation σ_Φ of the rotation phase shift yields,

$$\sigma_\Phi^2 = \frac{1}{4C^2}\left[2\alpha + \frac{1}{4}\left(\frac{1}{N^A} + \frac{1}{N^B} \right) + \gamma\left(\frac{1}{N^{A^2}} + \frac{1}{N^{B^2}} \right) \right].$$

$$(12)$$

The contrasts of the two interference fringes are identical for the two interferometers, and denoted by C. The coefficients α and γ are related to the detection features and were determined in Sec. II C 2. In order to characterize the contribution of the detection noise, it is convenient to plot the rotation phase noise versus the number of atoms. For a given
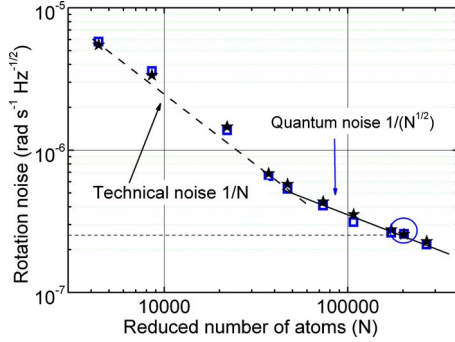
FIG. 14. (Color online) Rotation noise at 1 s measured on the interferometer (blue squares) and estimated taking into account the parameters of the detection system (stars) as a function of reduced atom number. The circle shows the usual parameters of the experiment corresponding to a reduced number of 2×10^5 atoms per shot.

loading time, the number of trapped atoms is different for the two atomic sources A and B, so we define a reduced atom number $N = \frac{N_A N_B}{N_A + N_B}$. Thus Eq. (12) becomes

$$\sigma_\Phi^2 \simeq \frac{1}{4C^2}\left(2\alpha + \frac{1}{4N} + \frac{\gamma}{N^2}\right). \tag{13}$$

In Fig. 14 the rotation noise (blue squares) is displayed versus reduced atom number. The data correspond to the Allan standard deviation at 1 s of the rotation phase shift calculated from series of 10 min of measurements. The black stars correspond to the noise estimated from Eq. (13) in which the coefficients α, γ were measured independently of the interferometric measurement (Sec. II C 2). We note excellent agreement between rotation noise measured with the
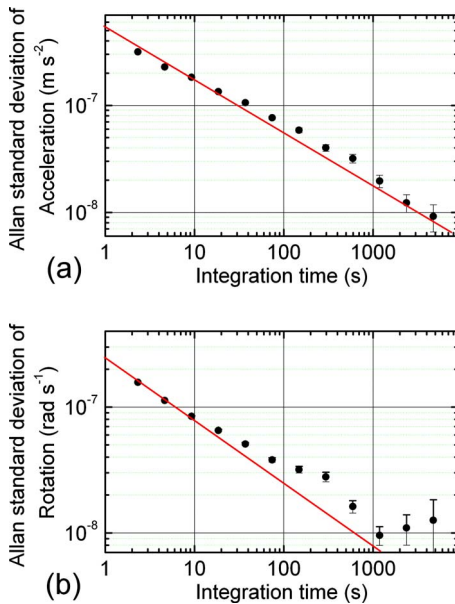

FIG. 15. (Color online) Allan standard deviation calculated for acceleration (a) and rotation (b) measurements (dots) from a 34 h continuous acquisition. The lines show the expected improvement of the sensitivity proportional to $\tau^{-1/2}$

two interferometers and the detection noise evaluated independently.

The number of atoms in the usual conditions is indicated by the circle in Fig. 14, which corresponds to a rotation noise of 2.4×10^{-7} rad s^{-1} Hz$^{-1/2}$, limited by the quantum projection noise. An improvement by a factor of 45 on the atom number ($\sim 10^7$ atoms), would allow to reach the detection noise plateau independent of the atom number, estimated from the parameter γ to be 4×10^{-8} rad s^{-1} Hz$^{-1/2}$. Such a number of atoms is now obtained during the usual loading time of our interferometer by using a 2D MOT [32].

C. Long term stability

The long term sensitivity achieves a plateau at 10^{-8} rad s^{-1} for time scales longer than 1000 s. We have carried out a systematic study of all possible sources of drift, which can limit the sensitivity for longer measurement times. First, we have verified that the orientation of the sensitive rotation axis is stable in space. Second, we have quantified the effect of a possible drift from every systematic error source. Only the fluctuations of trajectories, coupled to the wave-front distortions of the Raman laser, can explain the observed drift. The typical position fluctuations (20 μm) and drift sensitivity of 10^{-9} rad s^{-1} μm^{-1} gives a typical limit of the order of 2.10^{-8} rad s^{-1}, in agreement with the observed value.

This main limitation can be reduced drastically by combining an improvement of the wave front of the Raman laser and a reduction of the position fluctuations. Placing the retro-reflection system ($\lambda/4$ + mirror) inside the vacuum chamber removes aberrations induced by the window, which represents the highest contribution. The stabilities of the trajectories can be improved by the use of other kinds of optical fibers (having better stability of the polarization) or an active stabilization of polarization and intensity of each cooling beam.

V. CONCLUSION

We carried out the characterization of a cold-atom gyroscope in terms of sensitivity, systematic errors and scale factor. A study of the scale factor demonstrated excellent linearity and stability, limited by the resolution due to the drift of the systematic effects. This first study of the limits of a gyroscope using cold atoms has already demonstrated a sensitivity at the level of the best commercial optical gyroscopes (fiber and ring laser gyroscopes). In other work, a 400 times better short term performance was demonstrated using an atomic beam interferometer [9]. However, considering both at short and long term sensitivity, our gyroscope is three times less sensitive than the best atomic one [10]. Moreover, this work has clearly identified the limits to the sensitivity, pointing the way to further improvements.

The short term sensitivity was dominated by the quantum projection noise thanks to the use of a double interferometer, which perfectly cancels the phase shift due to parasitic vibrations. The main contribution to the drift is related to the fluctuations of the atomic trajectories. When coupled to the

Raman wave-front distortions, these fluctuations also limit the long term stability of the rotation measurements. More generally, similar effects from wave-front distortions should appear in the other kinds of dual cold-atom interferometers, based on molasses techniques, such as the gravity gradiometers [22,23], or on in tests of the universality of free fall by comparing the accelerations of two clouds of different species [33,34].

Finally, these limits are not fundamental and can be improved by at least one order of magnitude through various improvements. The parasitic shifts due to wave-front distortions can be reduced by improving the quality of the optics and the stability of the launch velocities. Furthermore, their impact in terms of rotation rate can be reduced by modifying the geometry. Indeed, atoms can be launched in straighter trajectories with a higher longitudinal velocity as in Ref. [14] or by using the four pulse configuration previously demonstrated in Ref. [11], with a longer interaction time. In both cases, the area of the interferometer is significantly increased while keeping the phase shift due to wave-front distortions almost constant. Long term performance should then be improved to reach an expected level below 10^{-10} rad s^{-1}, as achieved with giant ring laser gyroscopes [35], opening the way to new fields of application for atomic gyroscopes.

APPENDIX: SEPARATION OF ACCELERATION AND ROTATION PHASE SHIFTS

As our apparatus measures simultaneously two independent effects (acceleration and rotation), it is crucial to quantify how these two phase shifts are discriminated by the dual interferometer technique. Since the experiment enables the measurement of the six axes of inertia [11], this characterization was carried out in the horizontal Raman configuration which enables us to easily vary the acceleration phase shift over a large range and in a controlled way. The best performances, using this configuration, have been presented in Ref. [36] and are summarized in the following section.

1. Horizontal Raman beam configuration

In the horizontal configuration, the retro-reflected Raman beam is orientated in the y direction so as to realize the two interferometers in the (xy) plane at the apex of the trajectories. Therefore the interferometric phase shift is sensitive to
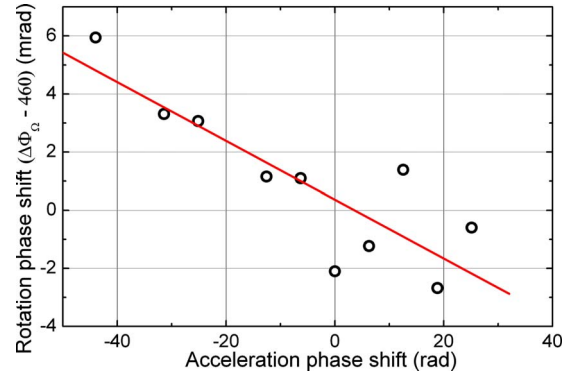

FIG. 16. (Color online) Measurement of the rotation phase shift as a function of the acceleration induced by varying the inclination of the interferometer plane. The measurements are performed in the horizontal Raman configuration with interferometers of $2T = 60$ ms of total interaction time. Each point corresponds to a measurement achieved for a given angle ε.

the horizontal acceleration a_y and the vertical rotation rate Ω_z. When the Raman beams are perfectly horizontal, the absolute value of the acceleration measured by the interferometer is close to zero while the rotation measurement records the vertical component of the Earth rotation rate $\Omega_z^E = 5.49 \times 10^{-5}$ rad s^{-1}.

This configuration allows inertial measurements with a total interaction time up to $2T = 60$ ms. Data are acquired in a similar way as in the vertical configuration, alternating measurements on the two sides of the central fringe, and for two opposite effective wave vectors. The short term sensitivity to rotation is 5.5×10^{-7} rad s^{-1} Hz$^{-1/2}$. The results are similar to those obtained on the vertical axis, taking in account the shorter interaction time T and the reduced contrast (20% instead of 30%).

2. Test of the separation

The horizontal configuration is well adapted to the measurement of the rejection of the acceleration phase shift on the rotation measurement. Indeed, as the interferometer is realized in the horizontal plane, it is possible to induce a large controlled change of the acceleration by tilting the device by an angle of ε with respect to the horizontal direction. The interferometer then measures a residual component of the gravitation g given by

$$\Delta\Phi_a = k_{\text{eff}} g \sin \varepsilon T^2. \tag{A1}$$

By tilting the interferometer plane over a range of 0.5 mrad, we change the acceleration phase shift from $\Delta\Phi_a = -45$ rad to 25 rad. Figure 16 displays the rotation phase shift as a function of the acceleration induced on the interferometer. The measurements exhibit a very small slope of 1.5×10^{-4}. Thus the effect of the acceleration on the rotation signal is cancelled at a level better than 76 dB.

This measurement demonstrates the efficiency of a dual interferometer gyroscope for applications in the presence of a relatively high level of acceleration noise.

[1] C. M. Will, Living Rev. Relativ. **9**, 3 (2006).

[2] H. Igel, A. Cauchard, J. Wassermann, A. Flaws, U. Schreiber, A. Velikoseltsev, and N. P. Dinh, Geophys. J. Int. **168**, 182 (2007).

[3] A. Lawrence, *Modern Inertial Technology* (Springer, New York, 1998).

[4] J. F. Clauser, Physica B **151**, 262 (1988).

[5] F. Riehle, Th. Kister, A. Witte, J. Helmcke, and Ch. J. Bordé, Phys. Rev. Lett. **67**, 177 (1991).

[6] M. Kasevich and S. Chu, Phys. Rev. Lett. **67**, 181 (1991).

[7] T. L. Gustavson, P. Bouyer, and M. A. Kasevich, Phys. Rev. Lett. **78**, 2046 (1997).

[8] A. Lenef, T. D. Hammond, E. T. Smith, M. S. Chapman, R. A. Rubenstein, and D. E. Pritchard, Phys. Rev. Lett. **78**, 760 (1997).

[9] T. L. Gustavson, A. Landragin, and M. A. Kasevich, Class. Quantum Grav. **17**, 2385 (2000).

[10] D. S. Durfee, Y. K. Shaham, and M. A. Kasevich, Phys. Rev. Lett. **97**, 240801 (2006).

[11] B. Canuel, F. Leduc, D. Holleville, A. Gauguet, J. Fils, A. Virdis, A. Clairon, N. Dimarcq, Ch. J. Bordé, A. Landragin, and P. Bouyer, Phys. Rev. Lett. **97**, 010402 (2006).

[12] S. Wu, E. Su, and M. Prentiss, Phys. Rev. Lett. **99**, 173201 (2007).

[13] P. Wang, R. B. Li, H. Yan, J. Wang, and M. S. Zhan, Chin. Phys. Lett. **24**, 27 (2007).

[14] T. Müller, M. Gilowski, M. Zaiser, P. Berg, Ch. Schubert, T. Wendrich, W. Ertmer, and E. M. Rasel, Eur. Phys. J. D **53**, 273 (2009).

[15] Ch. J. Bordé, Phys. Lett. A **140**, 10 (1989).

[16] Ch. Antoine and Ch. J. Bordé, J. Opt. B: Quantum Semiclassical Opt. **5**, S199 (2003).

[17] X. Baillard, A. Gauguet, S. Bize, P. Lemonde, Ph. Laurent, A. Clairon, and P. Rosenbusch, Opt. Commun. **266**, 609 (2006).

[18] F. Yver-Leduc, P. Cheinet, J. Fils, A. Clairon, N. Dimarcq, D. Holleville, P. Bouyer, and A. Landragin, J. Opt. B: Quantum Semiclassical Opt. **5**, S136 (2003).

[19] T. Lévèque, W. Chaibi, A. Gauguet, and A. Landragin (unpublished).

[20] G. Santarelli, Ph. Laurent, P. Lemonde, A. Clairon, A. G. Mann, S. Chang, A. N. Luiten, and C. Salomon, Phys. Rev. Lett. **82**, 4619 (1999).

[21] W. M. Itano, J. C. Bergquist, J. J. Bollinger, J. M. Gilligan, D. J. Heinzen, F. L. Moore, M. G. Raizen, and D. J. Wineland, Phys. Rev. A **47**, 3554 (1993).

[22] J. M. McGuirk, G. T. Foster, J. B. Fixler, M. J. Snadden, and M. A. Kasevich, Phys. Rev. A **65**, 033608 (2002).

[23] G. Lamporesi, A. Bertoldi, L. Cacciapuoti, M. Prevedelli, and G. M. Tino, Phys. Rev. Lett. **100**, 050801 (2008).

[24] Similar results have been observed in a gravimeter experiment [30] while atomic clouds are not launched but only dropped.

[25] D. S. Weiss, B. C. Young, and S. Chu, Appl. Phys. B: Lasers Opt. **59**, 217 (1994).

[26] K. Moler, D. S. Weiss, M. Kasevich, and S. Chu, Phys. Rev. A **45**, 342 (1992).

[27] A. Gauguet, T. E. Mehlstäubler, T. Lévèque, J. Le Gouët, W. Chaibi, B. Canuel, A. Clairon, F. Pereira Dos Santos, and A. Landragin, Phys. Rev. A **78**, 043615 (2008).

[28] J. Fils, F. Leduc, P. Bouyer, D. Holleville, N. Dimarcq, A. Clairon, and A. Landragin, Eur. Phys. J. D **36**, 257 (2005).

[29] J. Fils, Ph.D. thesis, Université Paris XI, 2002.

[30] J. Le Gouët, T. E. Mehlstäubler, J. Kim, S. Merlet, A. Clairon, A. Landragin, and F. Pereira Dos Santos, Appl. Phys. B: Lasers Opt. **92**, 133 (2008).

[31] L. Robertson *et al.*, Metrologia **38**, 71 (2001).

[32] K. Dieckmann, R. J. C. Spreeuw, M. Weidemüller, and J. T. M. Walraven, Phys. Rev. A **58**, 3891 (1998).

[33] R. A. Nyman, G. Varoquaux, F. Lienhart, D. Chambon, S. Boussen, J.-F. Clément, T. Müller, G. Santarelli, F. Pereira Dos Santos, A. Clairon, A. Bresson, A. Landragin, and P. Bouyer, Appl. Phys. B: Lasers Opt. **84**, 673 (2006).

[34] W. Ertmer *et al.*, Exp. Astron. **23**, 611 (2009).

[35] K. U. Schreiber, J.-P. R. Wells, and G. E. Stedman, Gen. Relativ. Gravit. **40**, 935 (2008).

[36] A. Landragin, B. Canuel, A. Gauguet, and P. Tuckey, Revue Française de Métrologie **10**, 11 (2007).